Nano Research 2015, 8(3): 808–820
DOI 10.1007/s12274-014-0563-3
Research Article

ISSN 1998-0124
CN 11-5974/O4

Ni-induced stepwise capacity increase in Ni-poor Li-rich cathode materials for high performance lithium ion batteries

Delai Ye[1], Chenghua Sun[2], Yu Chen[1], Kiyoshi Ozawa[3], Denisa Hulicova-Jurcakova[1], Jin Zou[4], and Lianzhou Wang[1] (✉)

[1] *Nanomaterials Centre, School of Chemical Engineering and Australian Institute of Bioengineering and Nanotechnology, The University of Queensland, Brisbane, QLD 4072, Australia*
[2] *School of Chemistry, Monash University, Clayton, Victoria 3800, Australia*
[3] *National Institute for Materials Science, Tsukuba, Ibaraki 305-0047, Japan*
[4] *Centre for Microscopy and Microanalysis and Material Engineering, The University of Queensland, Brisbane, QLD 4072, Australia*

Received: 11 June 2014
Revised: 3 August 2014
Accepted: 16 August 2014

KEYWORDS

Ni-doping,
capacity-increase,
Li-rich cathode materials,
lithium ion battery

ABSTRACT

Li-rich cathode materials have been considered as promising candidates for high-energy lithium ion batteries (LIBs). In this study, we report a new series of Li-rich materials ($Li[Li_{1/3-2x/3}Mn_{2/3-x/3}Ni_x]O_2$ ($0.09 \leqslant x \leqslant 0.2$)) doped with small amounts of Ni as cathode materials in LIBs, which exhibited unusual phenomenon of capacity increase up to tens of cycles due to the continuous activation of the Li_2MnO_3 phase. Both experimental and computational results indicate that unlike commonly studied Ni-doped Li-rich cathode materials, smaller amounts of Ni doping can promote the stepwise Li_2MnO_3 activation to obtain increased specific capacity and better cycling capability. In contrast, excessive Ni will over-activate the Li_2MnO_3 and result in a large capacity loss in the first cycle. The $Li_{1.25}Mn_{0.625}Ni_{0.125}O_2$ material with an optimized content of Ni delivered a superior high capacity of ~280 mAh·g^{-1} and good cycling stability at room temperature.

1 Introduction

Due to the high demands of electric vehicles and large-scale energy storage systems, rechargeable lithium ion batteries (LIBs) have received increasing attention as one of the best potential power sources for these applications [1–3]. Many new types of anode materials, such as Si [4] and some metal oxides [5, 6] have been developed as potential replacements for the conventional anode—graphite, and the newly introduced super-conductive graphene and its complexes with metal or metal oxides have demonstrated a superior high capacity of more than 1,000 mAh·g^{-1} with excellent rate performance [7–10]. However, the

---

Address correspondence to l.wang@uq.edu.au

current commercial cathode materials for LIBs, such as $LiCoO_2$ (140 mAh·g^{-1}), $LiMn_2O_4$ (120 mAh·g^{-1}) and $LiFePO_4$ (160 mAh·g^{-1}) are still far from satisfactory in terms of their low energy density and high cost [11–14], which has led to intensive efforts devoted to the exploration of new alternatives.

Li-rich layered oxides are a family of high energy cathode materials, which have been studied in recent years following the pioneering work by Thackeray [15, 16]. Generally, they are complex composites consisting of two highly integrated layered structures with the composition of Li_2MnO_3 ($C2/m$) and $LiMO_2$ ($R\bar{3}m$) and can deliver a high specific capacity of more than 250 mAh·g^{-1} (M = Ni, Co, Mn or their combination) [16–19]. Within this category of materials, a series of composites with the composition of $Li[Li_{1/3-2x/3}Mn_{2/3-x/3}Ni_x]O_2$ are of particular interest due to the absence of expensive and toxic Co. Much effort has been committed to revealing the relationships between the composition, atomic structure and the corresponding electrochemistry performance [20–29].

It has been generally accepted that Ni-doping can concurrently provide high voltage and improve the thermal stability of the layered cathode materials. On the other hand, in the case of the Li-rich materials, the high capacities arise mainly from the activation of the Li_2MnO_3 component, so the content of Ni should be limited in order to achieve high specific capacity. In addition, as the increased Ni content may substitute Li in the Li layer and lower the Li^+ mobility, minimizing the Ni content also favors improved rate performance [28, 30–32]. Considering all the above factors, particularly the working voltage and specific capacity, it is essential to maintain a balanced level of Ni in the Li-rich cathode materials to maximize the energy density. However, only the Ni/Mn ratios between 1/3 and 1/1 have been extensively studied in Li–Mn–Ni–O system to date [20, 21, 23–29, 32–34] while the performances of such composites with Ni/Mn ratios less than 1/3 have not been systematically explored so far.

Herein we report a series of intentionally designed Ni-poor Li-rich cathode materials $Li[Li_{1/3-2x/3}Mn_{2/3-x/3}Ni_x]O_2$ ($0.09 \leqslant x \leqslant 0.2$) where the Ni/Mn ratios are specified to be 1/7, 1/6, 1/5, 1/4 and 1/3, respectively (abbreviated as Ni/7, Ni/6, Ni/5, Ni/4 and Ni/3). Very interestingly, unlike the previously reported highly Ni-doped Li-rich materials with gradually declining capacities, the capacities of our materials were relatively small in the first cycle but continuously increased in the following tens of cycles to reach a maximum value of up to 280 mAh·g^{-1}. Detailed structure characterization confirmed that the continuous capacity increase is due to the gradual evolution of the Li_2MnO_3 phase, which is very different from the commonly studied Ni-doped Li-rich materials. More importantly, the substantial capacity loss in the first cycle that is commonly observed in Li-rich materials was significantly retarded in our optimized Ni/5 samples, leading to a remarkably high capacity. In addition, the undesirable large oxygen release in conventional Li-rich materials in the first cycle can also be substantially suppressed in our Ni-poor materials.

2 Experimental

2.1 Materials synthesis

All reagents were obtained from Sigma Aldrich. The $Li[Ni_xLi_{1/3-2x/3}Mn_{2/3-x/3}]O_2$ (x = 0.091, 0.105, 0.125, 0.154, 0.2) cathode materials were synthesized in two steps. In a typical synthesis, stoichiometric amounts of $Mn(NO_3)_2$ and $Ni(NO_3)_2$ were dissolved in distilled water and then co-precipitated with an equal volume of 0.2 M sodium carbonate solution. After stirring for 20 h at room temperature, the light brown precipitate was filtered, washed and dried at 100 °C. In the next step, the collected precipitate was pre-heated at 500 °C in air for 5 h and then calcined with a stoichiometric amount of $LiOH \cdot H_2O$ at 900 °C in air for another 12 h to obtain the final products.

2.2 Materials characterization

The mole ratio of the metal elements in each sample was determined by a Varian 725-ES inductively coupled plasma atomic emission spectrometer (ICP-AES). Crystalline structures of powder samples and electrodes were measured by X-ray diffraction (XRD) on a Bruker ADVANCE X-ray diffractometer (40 kV, 30 mA) with Cu Kα (λ = 0.15406 nm) radiation at a scanning rate of 1 °·min^{-1}. Morphological characteristics of the samples were investigated using a field-emission scanning electron microscope (FE-SEM, JEOL 7800). Transmission electron microscopy (TEM) investigations were conducted on a Philips FEI Tecnai F20 microscope operated at 200 kV.

2.3 Electrochemical tests

All the electrochemical tests were conducted in CR2032 coin cells at room temperature. Firstly, a working electrode was prepared by the doctor blade process. The active materials, acetylene black and polyvinylidene fluoride were mechanically mixed in the weight ratio of 7:2:1 with an appropriate amount of *N*-methyl-2-pyrrolidone. After that, the slurry was coated onto an aluminum foil (0.7 cm^2) and then dried in a vacuum oven at 120 °C for 12 h. The prepared working electrode was fabricated into CR2032 coin cells in an argon-filled glove box. Lithium foil and 1 M $LiPF_6$ in a mixture of ethylene carbonate (EC) and dimethyl carbonate (DMC) (1:1) were used as the negative electrode and electrolyte, respectively. The galvanostatic charge/discharge tests were performed using a multi-channel battery tester (Land CT2001A). The cyclic voltammetry (CV) measurements were conducted on a CHI660E electrochemical workstation.

2.4 Computational method

The Perdew–Burke–Ernzerhof functional embedded in the Vienna *ab initio* simulation package (VASP) was employed for the periodic density functional theory (DFT) calculations, and the projector augmented wave method with a cutoff energy of 380 eV was adopted to describe the electron–ion interactions [35–37]. The k-space was sampled by the gamma point. As it is associated with oxygen vacancies (OV), on-site electron correlation is essential and the DFT plus Hubbard model (DFT + U) was consequently employed in this work with the U valued at 5.0 eV for Mn and Co atoms [38–40]. A 2 × 1 × 2 supercell was built to model Li_2MnO_3 with the dimensions of 9.87 Å × 8.53 Å × 10.06 Å and formula of $Li_{32}Mn_{16}O_{48}$. OVs were represented by extracting one O-atom from the lattice while transition metal (TM) doping involves replacing an Mn-atom with another TM atom. The OV formation energy (E_f) was calculated by $E_f = E(Li_xMn_{16-\delta}TM_\delta O_{48}) - E(Li_xMn_{16-\delta}TM_\delta O_{47}) - {}^1\!/_2E(O_2)$. A negative value of E_f means that the formation of OV is endothermic.

3 Results and discussion

The mole ratios of Mn/Ni and Li/(Mn+Ni) for the $Li[Ni_xLi_{1/3-2x/3}Mn_{2/3-x/3}]O_2$ materials determined by ICP analysis are shown in Table S1 (in the Electronic Supplementary Material (ESM)). As indicated, the Ni/Mn ratios are consistent with the nominal values, indicating that the stoichiometry of the final products is close to the expected composition. XRD patterns of all the pristine samples (Fig. 1(a)) showed that all the Ni-doped cathode materials are highly crystalline and the structures are nearly identical to each other. The main diffraction peaks can be well indexed to the $R\bar{3}m$ space group (JCPDS No. 84–1634) with a typical layered phase. Some minor peaks appeared between 20° and 25°, which can be indexed to be the localized $LiMn_6$ superlattice in the monoclinic Li_2MnO_3-like regions [41–43]. In addition, a much higher intensity of the (003) peak relative to that of the (104) peak was observed, indicating a low degree of cation mixing in the Li layers. This phenomenon was also demonstrated by the well split pairs of (006)/(012) and (018)/(110) peaks [30]. These Ni-doped Li-rich cathode materials exhibited very similar microstructure and morphology as observed by the FE-SEM (Fig. S1 (in the ESM)). Particles having spherical morphology and a diameter of 2–3 μm were detected, with a hierarchical porous structure formed by the assembly of nano-sized sub-units homogeneously distributed over the whole microparticles. Such a hierarchical microstructure is very favorable for cathode materials because the primary nanoparticles can concurrently offer a large surface area for electrode–electrolyte contact and shorten the path for Li^+ diffusion [44–46]. Meanwhile, such a porous structure can effectively release the lattice strain and volume variation caused by the long period Li^+ intercalation/deintercalation reaction during the charge–discharge process.

To compare the electrochemical performance of these Ni-doped materials, they were initially cycled at 30 $mA\cdot g^{-1}$ (0.1C) between 2 and 4.8 V for 150 cycles. As shown in Fig. 1(b), the discharge capacities increase in the first few cycles. However, the rate and extent of the capacity increase are significantly different from each other. Ni/3, Ni/4 and Ni/5 samples become fully activated and reach their maximum capacity in

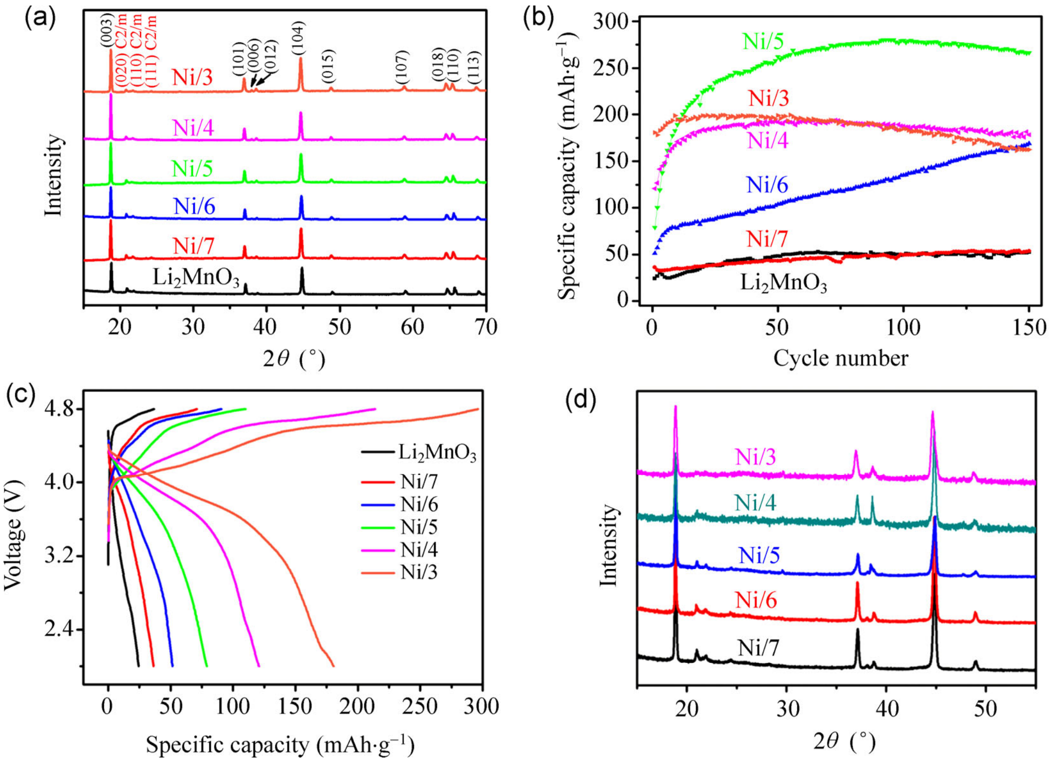

Figure 1 (a) XRD patterns of pristine cathode materials with different Ni-doping contents; (b) cycling performance of the cathode materials in the first 150 cycles at 30 mA·g^{-1} between 2.0–4.8 V; (c) the relevant 1st charge and discharge curves of Ni-doped cathode materials at 30 mA·g^{-1} between 2.0–4.8 V; (d) XRD patterns of the electrodes after the 1st cycle.

the 9th, 35th and 92th cycle, respectively. For the Ni/6 sample, the capacity increased almost linearly in the first 150 cycles and reached 169 mAh·g^{-1}. In contrast, for the samples of Ni/7 and the pure Li_2MnO_3, the capacities were almost unchanged and remained below 60 mAh·g^{-1}, similar to the values reported under the same conditions [47, 48]. Apparently, higher amounts of Ni-doping can lead to a faster capacity increase. More interestingly, the best performance was observed in the Ni/5 composite with a medium-low level of Ni doping. A specific discharge capacity of 279.6 mAh·g^{-1} could be achieved in the 100th cycle and well retained (>95%) after 150 cycles. Such a high discharge capacity and cycling stability is competitive with—or even better than—those reported for materials with higher content of Ni-doping and extra surface coating [49, 50], offering the possibility of designing high energy Li-rich cathode materials with less Ni using uncomplicated procedures.

Figure 1(c) shows the first charge/discharge curves of all samples. Both the first charge and discharge capacities increased with increasing content of Ni doping. Specifically, it can be found that the charge curves were composed of two plateaus—one at 4.0–4.6 V and the other at 4.6–4.8 V, both of which are extended as the Ni content increases. The first one at 4.0–4.6 V can be attributed to the oxidation reaction of the Ni^{2+} and Ni^{3+} ions to Ni^{4+} (possibly also to minor amounts of residual Mn^{3+} ions), and extended as a result of increasing Ni content [29]. The second one above 4.6 V corresponds to the activation process of the Li_2MnO_3 phase that is generally considered to involve simultaneous O extraction from the crystal lattice, further Li^+ extraction and rearrangement of the TM ions [16, 28, 29]. As the Ni content increased, this plateau was significantly stretched, indicating that more Li_2MnO_3 was activated in the first charging process. In addition, it is noted that as the Ni content increased, the capacity loss in the first cycle also increased. The Ni/3 sample showed the most serious capacity loss of 116 mAh·g^{-1} in the first cycle, which is 23 and 85 mAh·g^{-1} higher than the values for the Ni/4 and Ni/5 sample, respectively. Such a high capacity loss can be attributed to the major structural evolution—including lattice O removal and TM ion rearrangement–during the Li_2MnO_3 activation of materials with large content of dopants [18, 29, 34, 48]. By checking the columbic efficiency of these materials in the first 150 cycles (Fig. S2, in the ESM), it can be seen that the efficiencies increased markedly in the 2nd cycle and quickly reached ~100%, indicating that the extra capacity generated from the Li_2MnO_3 activation is almost 100% reversible from the 2nd cycle onwards. It has been reported that a higher capacity can be achieved if the upper voltage limit for Li_2MnO_3 activation is reached in a stepwise manner over a few cycles, and the capacity loss is caused by the diffusion of TM ions into the Li^+ vacancies during the activation process [51]. Our results are consistent with these earlier results. The high efficiency from the 2nd cycle onwards in our materials could be explained by the much smaller extent of Li_2MnO_3 activation in the subsequent cycles, which can significantly decrease the chance of Li^+ vacancies being occupied by the diffused TM ions.

XRD patterns of these materials after the first cycle are shown in Fig. 1(d). The weak diffraction peaks located between 20°–25° that reflect the Li–Mn ordering in the TM ion layers become gradually weaker in the more highly Ni-doped materials and almost disappear for the Ni/3 electrode, further confirming the effect of Ni doping in promoting the Li_2MnO_3 activation.

From the above discussion, it can be deduced that the electrochemical behavior of these Li-rich materials is closely related to their Ni content. Therefore, simulation studies were conducted to compare Ni and a variety of neighboring TM ions in terms of their influence on the energy barriers of TM ion diffusion and the formation of O vacancies (Fig. 2). In most Li-rich cathode materials, the first charge can be generally divided into two regions [16, 49]. When the voltage is below 4.5 V, all the TM ions like Co^{3+}, Ni^{2+} are oxidized, with Li ions being simultaneously removed from the Li layers, leaving local empty octahedral sites. As the charging voltage is continuously raised over 4.5 V, the Li_2MnO_3 phase will be gradually activated. This complex high voltage process involves a few sub-reactions, including the diffusing of Li and TM ions from the TM ion layers to the Li layers, the removal of lattice O ions and further Li extraction. As the aim

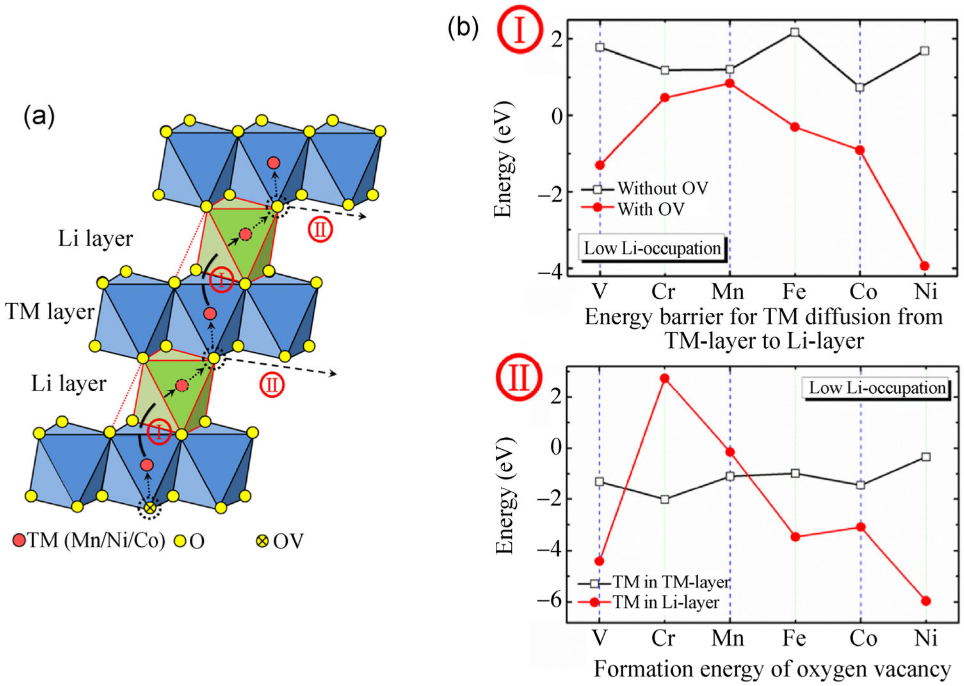

Figure 2 (a) Schematic illustration of TM ion diffusion and formation of oxygen vacancies in Li-rich materials; (b) the relevant energy barriers as a function of different TM ions.

of this work is to study the effect of Ni on the Li_2MnO_3 activation process that only happens in the high voltage region with some local Li vacancies in the Li layers, it is assumed in our simulation that the octahedral sites in the Li layers are empty [52].

In ideal pristine materials, no oxygen vacancies exist and TM ions only reside in their own layers. The energy barriers for the two sub-reactions of Li_2MnO_3 activation in this condition can be reflected by the white squares of the right hand side figures in Fig. 2. Diffusion of both the Mn and Ni is very restricted and they have a very limited effect on the promotion of the formation of oxygen vacancies. This can explain why the un-doped Li_2MnO_3 sample and Ni/7 sample both had very small capacity. As it has been reported that the amount of Ni in the Li layer drops significantly as the total Ni content decreases [27, 31, 32], it is reasonable to infer that the Ni/7 and Li_2MnO_3 samples are close to the ideal model that has no TM ions in the Li layers, and therefore, only very limited capacity could be achieved in these two materials since almost no Li_2MnO_3 phase is being activated.

As the Ni content gradually increases, more Ni may exist in the Li layer. In this case, the energy barrier for the formation of oxygen vacancies drops significantly (from the white squares to the red spheres in Fig. 2) with a difference of about 6 eV. This is a huge change that will significantly promote oxygen removal. Like a chain reaction, the newly formed oxygen vacancies will in return help more Ni diffuse into the Li layers. As this process continues, a small increase in the Ni content may result into the activation of a large part of the Li_2MnO_3 phase. This assumption is in good agreement with the electrochemical performance of our Ni-doped materials. Although the Ni/(Mn+Ni) ratio was varied within a narrow range between 12.5% (Ni/7) and 25% (Ni/3), the extent of activation of the Li_2MnO_3 was significantly enhanced from nearly zero (Ni/7) to almost fully complete in the first cycle (Ni/3). In addition, it should be mentioned here that no capacity increase with increasing number of cycles has been observed for most reported Ni-doped material systems [20, 25, 53], which—based on our results—could be explained by the high Ni/Mn ratio (equal to, or larger than, 1/3) in these cases, which enabled the Li_2MnO_3 phase to be activated mainly in the first charge.

To further reveal sources of the superior electrochemical performance of the Ni/5 sample, more detailed analysis was conducted. Firstly, it can be found from the energy dispersive spectrum (EDS) mapping (Fig. 3) that Ni and Mn elements are homogeneously distributed over the whole spherical matrix, demonstrating the uniform doping of Ni into the Li-rich material. A well-crystallized layered structure with typical layer distance of around 0.47 nm was revealed by the high resolution TEM image (Fig. 4(a)). The related electron diffraction pattern along the [010] axis confirms the clear monoclinic structure of the Ni/5 sample (Fig. 4(b)).

As the Ni/5 sample was cycled for about 100 times to reach its maximum specific discharge capacity, the first 200 cycles of this sample are presented in Fig. 5(a), and demonstrate its good cycling stability. It is found that a high discharge capacity of more than 240 $mAh\cdot g^{-1}$ was delivered by the Ni/5 sample in the

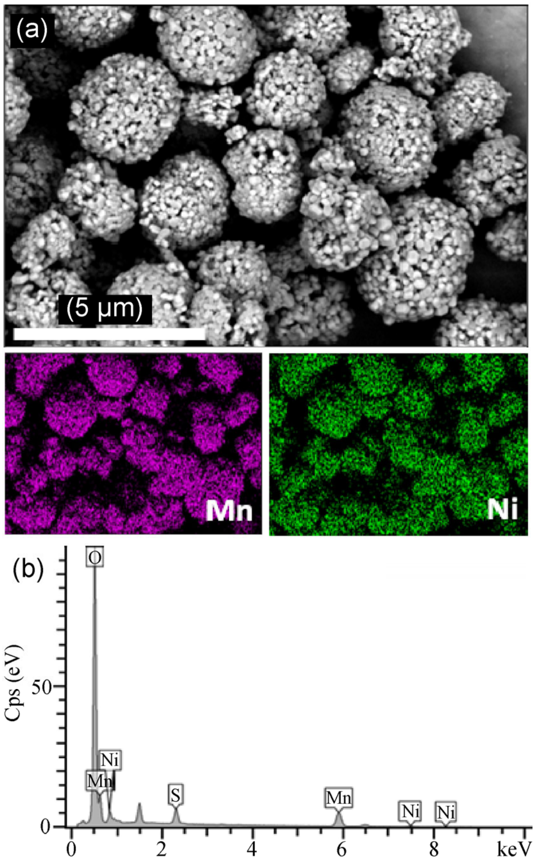

Figure 3 (a) SEM image and corresponding EDS mapping of Mn and Ni; (b) the corresponding EDS of the Ni/5 sample.

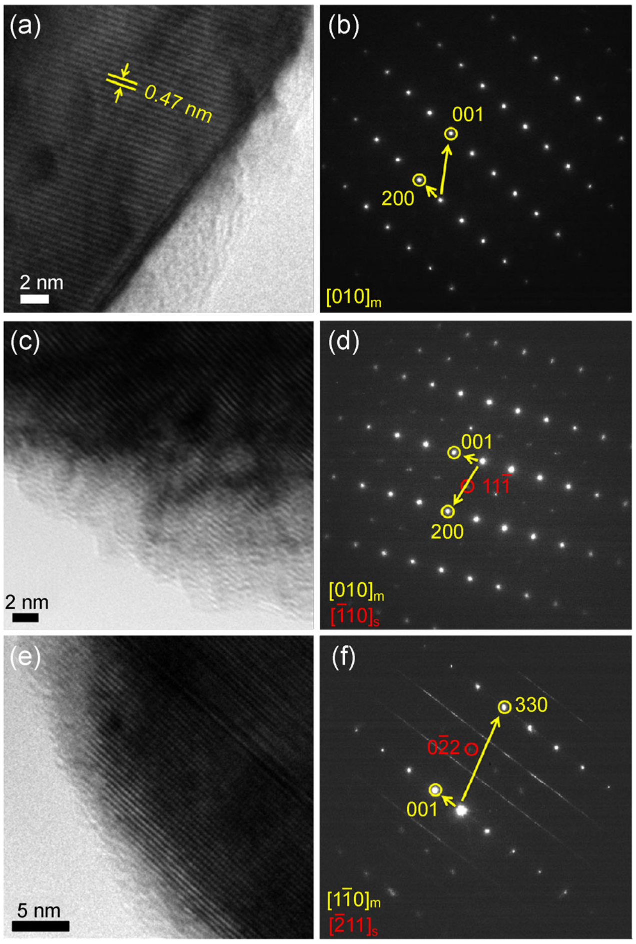

Figure 4 (a) HR-TEM image and (b) the corresponding electron diffraction pattern along the $[010]_{\text{mon}}$ axis of the pristine Ni/5 sample; (c) and (e) HR-TEM images and (d) and (f) the corresponding electron diffraction patterns along the $[010]_{\text{mon}}$ axis and $[1\bar{1}0]_{\text{mon}}$ axis of the Ni/5 electrode after 100 electrochemical cycles.

200th cycle. This value is about 86% of the peak capacity of 279.6 mAh·g^{-1}, demonstrating the high rate of capacity retention of this material. Such a capacity retention ratio compares very favorably with those for most reported Li-rich cathode materials with Ni doping under similar testing conditions [25, 45, 54]. It should be mentioned that the long activation time of around 100 cycles may not be advantageous for practical application, although the activation period could be controlled by further modifying the activation parameters. For example, a broad cycling potential window or a changed current density can speed up the Li_2MnO_3 activation process [55]. Fortunately, these parameters can be altered manually during the

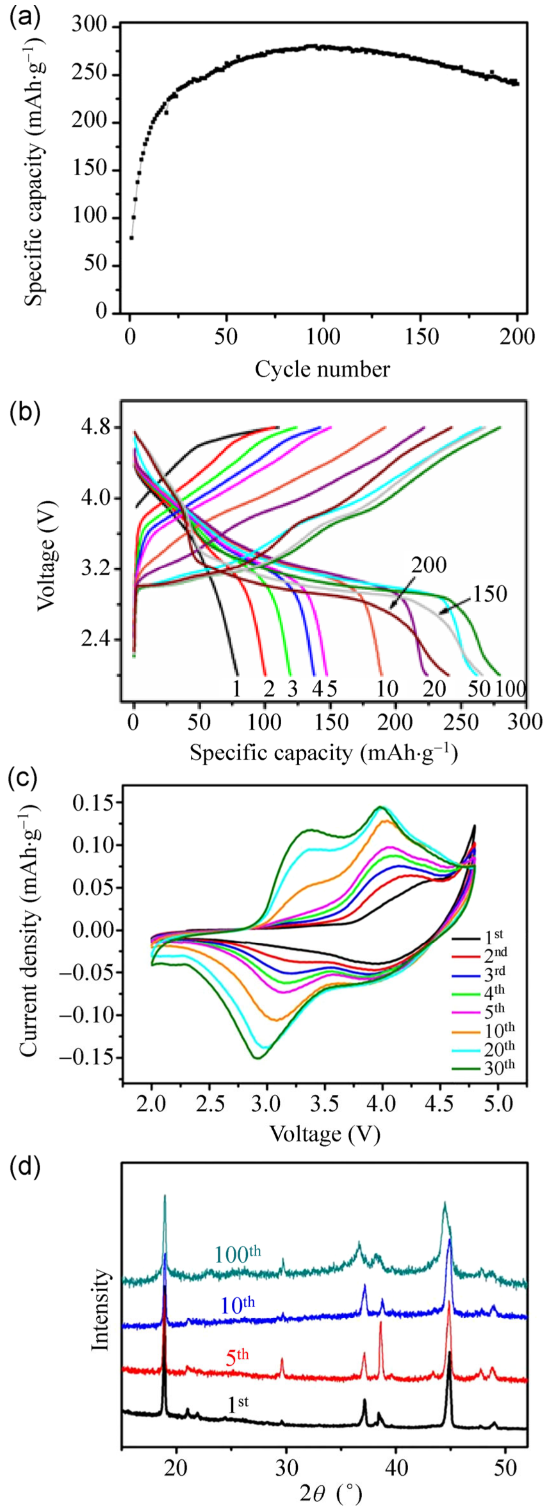

Figure 5 (a) Cycling performance of the Ni/5 material in the first 200 cycles at 30 mA·g^{-1} between 2.0–4.8 V; (b) and the corresponding charge/discharge curves of typical cycles; (c) CV curves of Ni/5 in different cycles at a scan rate of 0.02 mV·s^{-1}; (d) XRD patterns of the Ni/5 electrodes after different cycles.

electrochemical reactions to enhance the activation process and shorten the activation time. In addition, intentionally extending the high voltage charging period in the initial cycles, as shown below, could also be an effective way to tackle this problem.

Detailed charge/discharge plots of Ni/5 in different cycles are displayed in Fig. 5(b). It can be clearly seen that the 4.6–4.8 V charging plateau quickly faded after the first cycle and then quickly evolved into a long slope starting from around 3.6 V in the following cycles. This means a relatively high content of the Li_2MnO_3 phase was activated in the first cycle while the rest was gradually activated in a much reduced manner. The fast decline of the redox peaks located at around 4.8 V in the CV curves (Fig. 5(c)) further supports this varied manner of Li_2MnO_3 activation. In addition, a pair of flat charge and discharge plateaus centered at 3 V gradually evolved and finally became major feature in the first 150 cycles. This is also well reflected by the enlargement of the CV redox pairs at around 3 V, indicating that more Mn ions were involved in the electrochemical redox reactions and the structure was gradually transformed to the spinel phase [55–57]. Note that the discharge voltage plateau gradually declined over long term cycling of the Ni/5 sample (Figs. 5(b) and 5(c)). This phenomenon of voltage drop has also been observed in other Li-rich cathode materials [58, 59] and has generally been attributed to the diffusion of the TM ions into the Li layers, which may alter the crystallographic site energy for Li^+ occupation and enhance the phase transformation of the original layered phase to the spinel-like phase. This problematic voltage decay is of interest and can possibly be addressed by further optimizing the composition and surface modification, which is currently under detailed investigation. Good rate performance of the Ni/5 sample after the initial activation process has also been demonstrated, as shown in Fig. S3 (in the ESM). High specific discharge capacities of about 260, 222 and 182 $mAh \cdot g^{-1}$ were delivered at current densities of 60, 150 and 300 $mA \cdot g^{-1}$ respectively, which are competitive with other Li-rich cathode materials with higher contents of Ni [54, 57].

Ex situ XRD patterns of the Ni/5 electrodes after different cycles are shown in Fig. 5(d). It can be seen that the intensities of the characteristic peaks of Li_2MnO_3 at around 20°–25° gradually decreased upon cycling and the peaks totally disappeared after 100 cycles, further confirming the gradual consumption of the Li_2MnO_3 component. In addition, comparing the high resolution TEM (HR-TEM) images and related electron diffractions of the pristine Ni/5 sample and the electrode after 100 cycles (Fig. 4), reticulate patterns embedded on the pristine parallel lattice and new spots associated with the spinel phase were observed in the cycled samples along both the $[010]_{mon}$ and $[1\bar{1}0]_{mon}$ axes, strongly indicating that a new spinel phase, based on the parent layered structure, had been generated. This is consistent with the long 3 V discharge plateau and 3 V CV peak, which were also observed in other reported Li-rich materials as characteristic features of a defect spinel phase [15, 40, 50, 60]. The Electrochemical impedance spectroscopy (EIS) measurements of the Ni/5 material were also conducted (Fig. S4, in the ESM). It was found that the charge transfer resistance, that is related to the charge transfer on the electrode/electrolyte interface, gradually decreased during the activation process [61, 62]. This trend is in good agreement with the fact that more Li^+ is involved in the electrochemical reactions as the capacity increases during the activation process.

It is worth mentioning that the first charge plateau at 4.6–4.8 V in Ni/5 is much shorter than that for the Ni/3 and Ni/4 materials. This plateau quickly declined and vanished after the 5th cycle. It is well-known that this plateau indicates an oxygen-releasing reaction in Li-rich cathode materials, and the length is in proportion to the amount of O_2 generation [16, 27, 29, 63]. Therefore, it can be inferred that the O_2 generated in the Ni/5 material is much less than that for the Ni/3 and Ni/4 materials. As O_2 accumulation in batteries may bring safety concerns, some techniques such as surface coating or incorporating additives in the electrolyte have been adopted to eliminate the O_2 release [64, 65]. However, these complex approaches are time-consuming and expensive, which severely restricts their practical applications. Since our Ni/5 sample has the intrinsic property of producing much less O_2, it may bring us one step closer to a safer and cheaper Li-rich battery system.

Based on the above discussion, the fact that Ni/5 shows the highest capacity has two possible origins.

On the one hand, sufficient content of Ni doping is critical to fully activate the Li-rich phase in the first few cycles. On the other hand, too much Ni-doping may lead to excessive activation and consequently, a big capacity loss in the first cycle. Therefore, the optimized Ni/5 sample may benefit from its balanced level of Ni-doping and make maximum use of the capacity originating from the Li_2MnO_3 activation.

We hypothesize that excessive activation of Li_2MnO_3 in the first cycle may lead to large capacity loss due to the large-scale structure change and TM ion rearrangement. To test this hypothesis, we intentionally extended the activation time of the Ni/5 sample in the first cycle. That is, after the normal constant current charge to 4.8 V, the samples were continuously charged at 4.8 V for 4, 7 and 10 h respectively, followed by normal cycles. Initially, it can be clearly seen from Fig. 6(a) that the maximum capacity of the Ni/5 sample was significantly reduced after 4 h constant high-voltage charging in the first cycle. Then, it further decreased as the holding time lasted even longer. In addition, although all these over-charged electrodes still experienced a capacity increase in the subsequent cycles, the trend was much less marked than for the normal one. On the other hand, comparing the first charge and discharge curves only (Fig. 6(b)), it is found that both the charge and discharge capacities increased with prolonged 4.8 V charging. Meanwhile, the capacity loss in the first cycle was simultaneously enlarged as well.

All these observations support our hypothesis: During the extended 4.8 V charging process in the first cycle, much more Li_2MnO_3 phase was activated and consumed, leading to larger first charge/discharge capacity; meanwhile, as the Li_2MnO_3 activation becomes greater, more TM ions may diffuse and occupy the Li vacancies, resulting in a larger capacity loss. The accumulated lattice strain and extensive lattice O extraction associated with the large-scale Li_2MnO_3 activation process may increase the capacity loss even further. Therefore, in order to obtain a high specific capacity and suppress the capacity loss, aggressive activation of the Li_2MnO_3 phase in the first charge should be avoided in these materials.

The electrodes of the Ni/5 sample after the first cycle with different durations of 4.8 V charging were characterized by XRD (Fig. 6(c)). The intensity of the *C*2/*m* peaks at 20°–25° significantly decreased after holding the sample at 4.8 V charging for a few hours, providing structural evidence of the continuous activation of Li_2MnO_3 during this period. It should be noted that the intensity of these small peaks are not

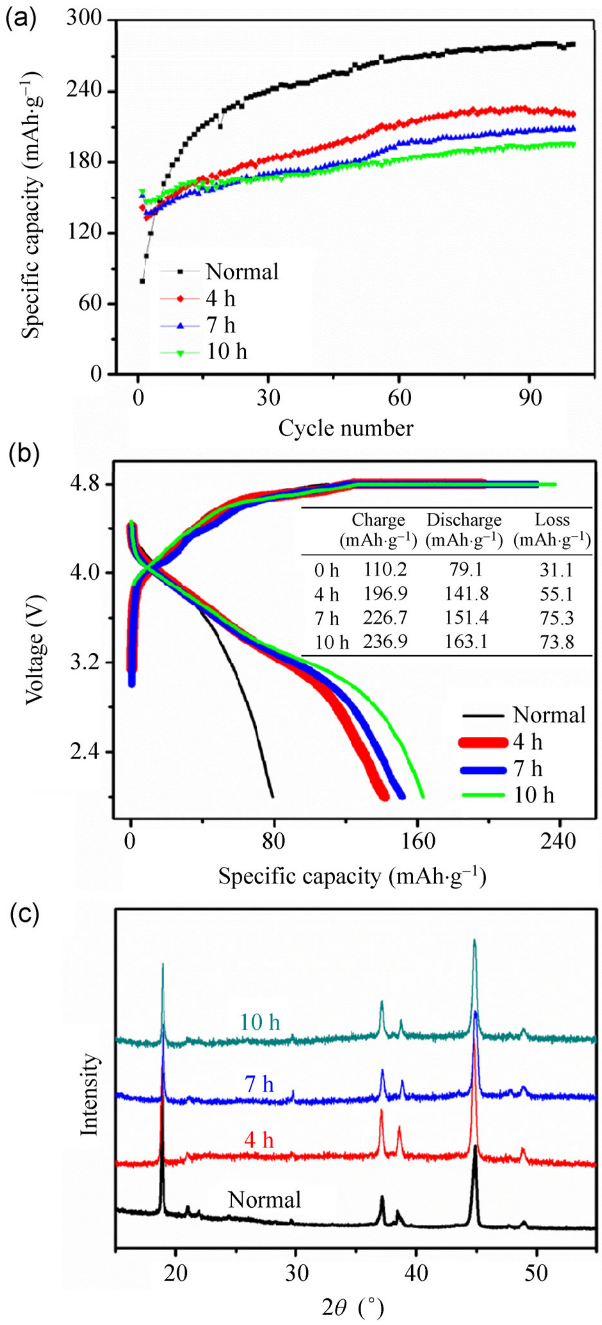

	Charge (mAh·g^{-1})	Discharge (mAh·g^{-1})	Loss (mAh·g^{-1})
0 h	110.2	79.1	31.1
4 h	196.9	141.8	55.1
7 h	226.7	151.4	75.3
10 h	236.9	163.1	73.8

Figure 6 (a) Cycling performance and (b) first charge and discharge curves of the Ni/5 electrode; (c) XRD patterns after the first cycle without (normal, 0 h) or with extended 4, 7 or 10 h of 4.8 V constant-voltage charging in the first cycle.

greatly further changed or disappeared when the 4.8 V charging of the Ni/5 electrode was further prolonged from 4 to 7 or 10 h. From Fig. 6(b), it can also be found that the increase in charge capacity from 4 to 10 h was very small and less than half of that from 0 to 4 h. This implies that 4 h charging at 4.8 V may be long enough to consume the majority of the Li_2MnO_3 phase.

Based on the above discussion, the relationship between the electrochemical behavior, Ni content and structure evolution of these Li-rich cathode materials can be summarized, as shown in Scheme 1. In high content Ni-doped materials (condition I), the majority of the Li_2MnO_3 phase will be used in the first cycle, leading to large scale structure change and associated atomic rearrangement. As a result, much of the capacity obtained from the Li_2MnO_3 activation then becomes irreversible. Conversely, in Li-rich materials with very low content of Ni or even no Ni (condition III), the Li_2MnO_3 cannot be activated effectively and the specific capacity will stay low. Here in our series of Ni-doped Li-rich composites, in terms of the specific capacity, a material with a medium-low level of Ni-doping (condition II) is favorable to kinetically activate the Li_2MnO_3 at a reasonable rate and—more importantly—limit the large capacity loss in the first cycle.

4 Conclusions

The composition, microstructure and electrochemical properties of a series of Ni-poor Li-rich cathode materials with the composition $Li[Li_{1/3-2x/3}Mn_{2/3-x/3}Ni_x]O_2$ ($0.09 \leqslant x \leqslant 0.2$) have been systematically investigated in an attempt to obtain high performance Li-rich cathode materials for LIBs. Compared to traditional Li-rich Li–Mn–Ni–O material systems with high Ni-doping content, our Li-rich cathode materials with optimized low content of Ni exhibited an unusual specific capacity increase in the first dozens of cycles due to the continuous activation of the Li_2MnO_3 phase upon cycling. Combining our experimental and computational results revealed that the Ni-doping can significantly promote the Li_2MnO_3 activation and provide extra specific capacity. However, excessive Ni-doping can lead to the undesirable excessive

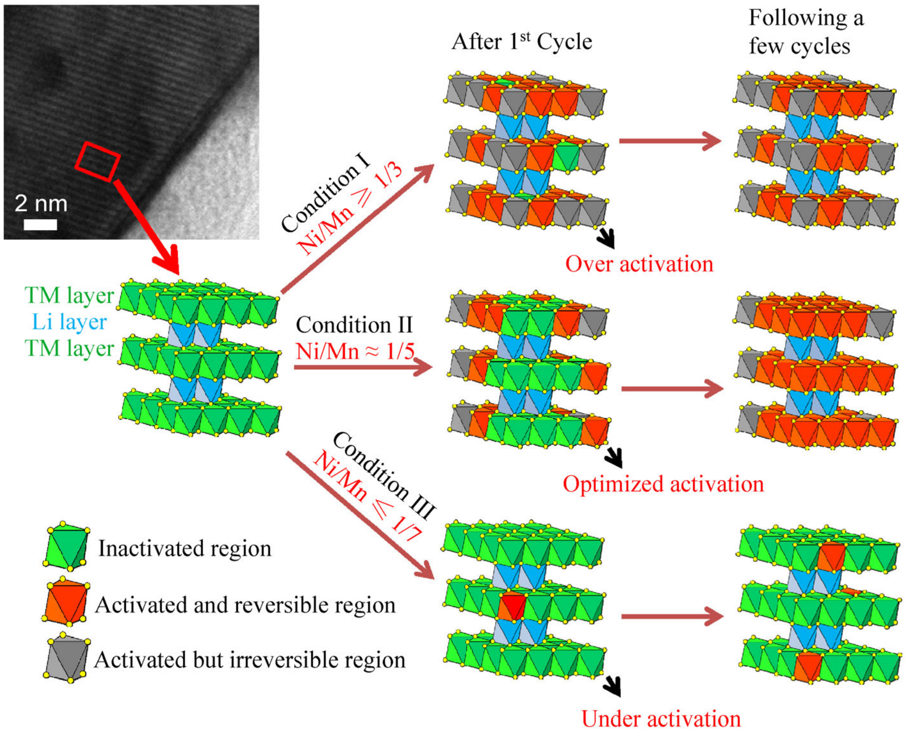

Scheme 1 Effect of over-activation, optimized activation and under-activation of the Li_2MnO_3 phase on the structure evolution and electrochemical behavior of layered Li-rich materials as a function of the content of Ni.

activation of the Li_2MnO_3 phase, with an associated substantial capacity loss, in the first cycle. As a result, the content of Ni in our low Ni Li-rich material systems was optimized in order to achieve a superior specific capacity (~280 mAh·g^{-1}) and good cycling stability at room temperature. This work can not only provide new insights into the fundamental understanding of the reaction mechanisms for Li-rich Li–Mn–Ni–O material systems, but also shed light on the design of cheaper and safer high-energy cathode materials for new generation LIBs.

Acknowledgements

D. L. Y. acknowledges financial support from Chinese Scholarship Council (CSC) and authors are grateful to ARC through its LP and DP programs. The authors also thank Mr. Zhi Zhang and Mr. Guang Han for the technical support in SEM and TEM characterization.

Electronic Supplementary Material: Supplementary material (ICP measurements, SEM imaging and columbic efficiency of the materials) is available in the online version of this article at http://dx.doi.org/10.1007/s12274-014-0563-3.

References

[1] Armand, M.; Tarascon, J. M. Building better batteries. *Nature* **2008**, *451*, 652–657.

[2] Dunn, B.; Kamath, H.; Tarascon, J. M. Electrical energy storage for the grid: A battery of choices. *Science* **2011**, *334*, 928–935.

[3] Liu, J. Addressing the grand challenges in energy storage. *Adv. Funct. Mater.* **2013**, *23*, 924–928.

[4] Chan, C. K.; Patel, R. N.; O'Connell, M. J.; Korgel, B. A.; Cui, Y. Solution-grown silicon nanowires for lithium-ion battery anodes. *ACS Nano* **2010**, *4*, 1443–1450.

[5] Jeong, G.; Kim, J. G.; Park, M. S.; Seo, M.; Hwang, S. M.; Kim, Y. U.; Kim, Y. J.; Kim, J. H.; Dou, S. X. Core–shell structured silicon nanoparticles@TiO_{2-x}/carbon mesoporous microfiber composite as a safe and high-performance lithium-ion battery anode. *ACS Nano* **2014**, *8*, 2977–2985.

[6] Kim, J. G.; Shi, D.; Park, M. S.; Jeong, G.; Heo, Y. U.; Seo, M.; Kim, Y. J.; Kim, J. H.; Dou, S. X. Controlled Ag-driven superior rate-capability of $Li_4Ti_5O_{12}$ anodes for lithium rechargeable batteries. *Nano Res.* **2013**, *6*, 365–372.

[7] Luo, B.; Wang, B.; Li, X.; Jia, Y.; Liang, M.; Zhi, L. Graphene-confined Sn nanosheets with enhanced lithium storage capability. *Adv. Mater.* **2012**, *24*, 3538–3543.

[8] Luo, B.; Wang, B.; Liang, M.; Ning, J.; Li, X.; Zhi, L. Reduced graphene oxide-mediated growth of uniform tin-core/carbon-sheath coaxial nanocables with enhanced lithium ion storage properties. *Adv. Mater.* **2012**, *24*, 1405–1409.

[9] Wang, H.; Cui, L. F.; Yang, Y.; Sanchez Casalongue, H.; Robinson, J. T.; Liang, Y.; Cui, Y.; Dai, H. Mn_3O_4–graphene hybrid as a high-capacity anode material for lithium ion batteries. *J. Am. Chem. Soc.* **2010**, *132*, 13978–13980.

[10] Wang, D.; Choi, D.; Li, J.; Yang, Z.; Nie, Z.; Kou, R.; Hu, D.; Wang, C.; Saraf, L. V.; Zhang, J. Self-assembled TiO_2–graphene hybrid nanostructures for enhanced Li-ion insertion. *ACS Nano* **2009**, *3*, 907–914.

[11] Goodenough, J. B. Electrochemical energy storage in a sustainable modern society. *Energy Environ. Sci.* **2014**, *7*, 14–18.

[12] Aricò, A. S.; Bruce, P.; Scrosati, B.; Tarascon, J. M.; Van Schalkwijk, W. Nanostructured materials for advanced energy conversion and storage devices. *Nat. Mater.* **2005**, *4*, 366–377.

[13] Xiao, X.; Lu, J.; Li, Y. $LiMn_2O_4$ microspheres: Synthesis, characterization and use as a cathode in lithium ion batteries. *Nano Res.* **2010**, *3*, 733–737.

[14] Armstrong, M. J.; O'Dwyer, C.; Macklin, W. J.; Holmes, J. D. Evaluating the performance of nanostructured materials as lithium-ion battery electrodes. *Nano Res.* **2014**, *7*, 1–62.

[15] Johnson, C.; Li, N.; Vaughey, J.; Hackney, S.; Thackeray, M. Lithium–manganese oxide electrodes with layered-spinel composite structures $xLi_2MnO_3–(1–x)Li_{1+y}Mn_{2–y}O_4$ ($0 < x < 1, 0 \leqslant y \leqslant 0.33$) for lithium batteries. *Electrochem. Commun.* **2005**, *7*, 528–536.

[16] Thackeray, M. M.; Kang, S. H.; Johnson, C. S.; Vaughey, J. T.; Benedek, R.; Hackney, S. Li_2MnO_3-stabilized $LiMO_2$ (M = Mn, Ni, Co) electrodes for lithium-ion batteries. *J. Mater. Chem.* **2007**, *17*, 3112–3125.

[17] Bareno, J.; Lei, C.; Wen, J.; Kang, S. H.; Petrov, I.; Abraham, D. Local structure of layered oxide electrode materials for lithium-ion batteries. *Adv. Mater.* **2010**, *22*, 1122–1127.

[18] Boulineau, A.; Simonin, L.; Colin, J. F. O.; Canévet, E.; Daniel, L.; Patoux, S. B. Evolutions of $Li_{1.2}Mn_{0.61}Ni_{0.18}Mg_{0.01}O_2$ during the initial charge/discharge cycle sudied by advanced electron microscopy. *Chem. Mater.* **2012**, *24*, 3558–3566.

[19] Yu, H.; Shikawa, R.; So, Y. G.; Shibata, N.; Kudo, T.; Zhou, H.; Ikuhara, Y. Direct atomic-resolution observation of two phases in the $Li_{1.2}Mn_{0.567}Ni_{0.166}Co_{0.067}O_2$ cathode material for lithium-ion batteries. *Angew. Chem.Int. Ed.* **2013**, *52*, 5969–5973.

[20] Lu, Z.; Beaulieu, L.; Donaberger, R.; Thomas, C.; Dahn, J. Synthesis, structure, and electrochemical behavior of $Li[Ni_xLi_{1/3-2x/3}Mn_{2/3-x/3}]O_2$. *J. Electrochem. Soc.* **2002**, *149*, A778–A791.

[21] Yoon, W. S.; Iannopollo, S.; Grey, C. P.; Carlier, D.; Gorman, J.; Reed, J.; Ceder, G. Local structure and cation ordering in O3 lithium nickel manganese oxides with stoichiometry $Li[Ni_xMn_{(2-x)/3}Li_{(1-2x)/3}]O_2$ NMR studies and first principles calculations. *Electrochem. Solid-State Lett.* **2004**, *7*, A167–A171.

[22] Jiang, J.; Dahn, J. Electrochemical and thermal studies of $Li[Ni_xLi_{(1/3-2x/3)}Mn_{(2/3-x/3)}]O_2$ (x = 1/12, 1/4, 5/12, and 1/2). *Electrochim. Acta* **2005**, *50*, 4778–4783.

[23] Park, S. H.; Kang, S. H.; Johnson, C.; Amine, K.; Thackeray, M. Lithium–manganese–nickel–oxide electrodes with integrated layered-spinel structures for lithium batteries. *Electrochem. Commun.* **2007**, *9*, 262–268.

[24] Lei, C.; Bareno, J.; Wen, J.; Petrov, I.; Kang, S. H.; Abraham, D. Local structure and composition studies of $Li_{1.2}Ni_{0.2}Mn_{0.6}O_2$ by analytical electron microscopy. *J. Power Sources* **2008**, *178*, 422–433.

[25] Fell, C. R.; Carroll, K. J.; Chi, M.; Meng, Y. S. Synthesis–structure–property relations in layered, "Li-excess" oxides electrode materials $Li[Li_{1/3-2x/3}Ni_xMn_{2/3-x/3}]O_2$ (x = 1/3, 1/4, and 1/5). *J. Electrochem. Soc.* **2010**, *157*, A1202–A1211.

[26] Gao, M.; Lian, F.; Liu, H.; Tian, C.; Ma, L.; Yang, W. Synthesis and electrochemical performance of long lifespan Li-rich $Li_{1+x}(Ni_{0.37}Mn_{0.63})_{1-x}O_2$ cathode materials for lithium-ion batteries. *Electrochim. Acta* **2013**, *95*, 87–94.

[27] Jarvis, K. A.; Wang, C. C.; Manthiram, A.; Ferreira, P. J. The role of composition in the atomic structure, oxygen loss, and capacity of layered Li–Mn–Ni oxide cathodes. *J. Mater. Chem. A* **2014**, *2*, 1353–1362.

[28] Xu, B.; Fell, C. R.; Chi, M.; Meng, Y. S. Identifying surface structural changes in layered Li-excess nickel manganese oxides in high voltage lithium ion batteries: A joint experimental and theoretical study. *Energy Environ. Sci.* **2011**, *4*, 2223–2233.

[29] Armstrong, A. R.; Holzapfel, M.; Novák, P.; Johnson, C. S.; Kang, S. H.; Thackeray, M. M.; Bruce, P. G. Demonstrating oxygen loss and associated structural reorganization in the lithium battery cathode $Li_{1.2}Ni_{0.2}Mn_{0.6}O_2$. *J. Am. Chem. Soc.* **2006**, *128*, 8694–8698.

[30] Schougaard, S. B.; Bréger, J.; Jiang, M.; Grey, C. P.; Goodenough, J. B. $LiNi_{0.5+\delta}Mn_{0.5-\delta}O_2$—A high-rate, high-capacity cathode for lithium rechargeable batteries. *Adv. Mater.* **2006**, *18*, 905–909.

[31] Lu, Z.; Chen, Z.; Dahn, J. Lack of cation clustering in $Li[Ni_xLi_{1/3-2x/3}Mn_{2/3-x/3}]O_2$ ($0 < x \leqslant 1/2$) and $Li[Cr_xLi_{(1-x)/3}Mn_{(2-2x)/3}]O_2$ ($0 < x < 1$). *Chem. Mater.* **2003**, *15*, 3214–3220.

[32] Meng, Y.; Ceder, G.; Grey, C.; Yoon, W. S.; Jiang, M.; Breger, J.; Shao-Horn, Y. Cation ordering in layered O_3 $Li[Ni_xLi_{1/3-2x/3}Mn_{2/3-x/3}]O_2$ ($0 \leqslant x \leqslant 1/2$) compounds. *Chem. Mater.* **2005**, *17*, 2386–2394.

[33] Lu, Z.; MacNeil, D.; Dahn, J. Layered cathode materials $Li[Ni_xLi_{(1/3-2x/3)}Mn_{(2/3-x/3)}]O_2$ for lithium-ion batteries. *Electrochem. Solid-State Lett.* **2001**, *4*, A191–A194.

[34] Lu, Z.; Dahn, J. R. Understanding the anomalous capacity of $Li/Li[Ni_xLi_{(1/3-2x/3)}Mn_{(2/3-x/3)}]O_2$ cells using *in situ* X-ray diffraction and electrochemical studies. *J. Electrochem. Soc.* **2002**, *149*, A815–A822.

[35] Perdew, J. P.; Burke, K.; Ernzerhof, M. Generalized gradient approximation made simple. *Phys. Rev. Lett.* **1996**, *77*, 3865–3868.

[36] Blöchl, P. E. Projector augmented-wave method. *Phys. Rev. B* **1994**, *50*, 17953–17979.

[37] Kresse, G.; Joubert, D. From ultrasoft pseudopotentials to the projector augmented-wave method. *Phys. Rev. B* **1999**, *59*, 1758–1775.

[38] Anisimov, V. I.; Zaanen, J.; Andersen, O. K. Band theory and Mott insulators: Hubbard U instead of Stoner I. *Phys. Rev. B* **1991**, *44*, 943–954.

[39] Chevrier, V. L.; Ong, S. P.; Armiento, R.; Chan, M. K.; Ceder, G. Hybrid density functional calculations of redox potentials and formation energies of transition metal compounds. *Phys. Rev. B* **2010**, *82*, 075122.

[40] Hinuma, Y.; Meng, Y. S.; Kang, K.; Ceder, G. Phase transitions in the $LiNi_{0.5}Mn_{0.5}O_2$ system with temperature. *Chem. Mater.* **2007**, *19*, 1790–1800.

[41] Kang, S. H.; Kempgens, P.; Greenbaum, S.; Kropf, A.; Amine, K.; Thackeray, M. Interpreting the structural and electrochemical complexity of $0.5Li_2MnO_3\cdot 0.5LiMO_2$ electrodes for lithium batteries ($M = Mn_{0.5-x}Ni_{0.5-x}Co_{2x}$, $0 \leqslant x \leqslant 0.5$). *J. Mater. Chem.* **2007**, *17*, 2069–2077.

[42] Bréger, J.; Jiang, M.; Dupré, N.; Meng, Y. S.; Shao-Horn, Y.; Ceder, G.; Grey, C. P. High-resolution X-ray diffraction, DIFFaX, NMR and first principles study of disorder in the Li_2MnO_3–$Li[Ni_{1/2}Mn_{1/2}]O_2$ solid solution. *J. Solid State Chem.* **2005**, *178*, 2575–2585.

[43] Jarvis, K. A.; Deng, Z.; Allard, L. F.; Manthiram, A.; Ferreira, P. J. Atomic structure of a lithium-rich layered oxide material for lithium-ion batteries: Evidence of a solid solution. *Chem. Mater.* **2011**, *23*, 3614–3621.

[44] He, X.; Wang, J.; Kloepsch, R.; Krueger, S.; Jia, H.; Liu, H.; Vortmann, B.; Li, J. Enhanced electrochemical performance in lithium ion batteries of a hollow spherical lithium-rich cathode material synthesized by a molten salt method. *Nano Res.* **2014**, *7*, 110–118.

[45] Shi, S.; Tu, J.; Zhang, Y.; Zhang, Y.; Gu, C.; Wang, X. Morphology and electrochemical performance of $Li[Li_{0.2}Mn_{0.56}Ni_{0.16}Co_{0.08}]O_2$ cathode materials prepared with different metal sources. *Electrochim. Acta* **2013**, *109*, 828–834.

[46] Shi, S.; Lou, Z.; Xia, T.; Wang, X.; Gu, C.; Tu, J. Hollow $Li_{1.2}Mn_{0.5}Co_{0.25}Ni_{0.05}O_2$ microcube prepared by binary template as a cathode material for lithium ion batteries. *J. Power Sources* **2014**, *257*, 198–204.

[47] Denis, Y.; Yanagida, K.; Kato, Y.; Nakamura, H. Electrochemical activities in Li_2MnO_3. *J. Electrochem. Soc.* **2009**, *156*, A417–A424.

[48] Robertson, A. D.; Bruce, P. G. Mechanism of electrochemical activity in Li_2MnO_3. *Chem. Mater.* **2003**, *15*, 1984–1992.

[49] Wang, R.; He, X.; He, L.; Wang, F.; Xiao, R.; Gu, L.; Li, H.; Chen, L. Atomic structure of Li_2MnO_3 after partial delithiation and re-lithiation. *Adv. Energy Mater.* **2013**, *3*, 1358–1367.

[50] Sun, Y. K.; Lee, M. J.; Yoon, C. S.; Hassoun, J.; Amine, K.; Scrosati, B. The role of AlF_3 coatings in improving electrochemical cycling of Li-enriched nickel–manganese oxide electrodes for Li-ion batteries. *Adv. Mater.* **2012**, *24*, 1192–1196.

[51] van Bommel, A.; Krause, L.; Dahn, J. Investigation of the irreversible capacity loss in the lithium-rich oxide $Li[Li_{1/5}Ni_{1/5}Mn_{3/5}]O_2$. *J. Electrochem. Soc.* **2011**, *158*, A731–A735.

[52] Lee, J.; Urban, A.; Li, X.; Su, D.; Hautier, G.; Ceder, G. Unlocking the potential of cation-disordered oxides for rechargeable lithium batteries. *Science* **2014**, *343*, 519–522.

[53] Ohzuku, T.; Nagayama, M.; Tsuji, K.; Ariyoshi, K. High-capacity lithium insertion materials of lithium nickel manganese oxides for advanced lithium-ion batteries: Toward rechargeable capacity more than 300 $mAh \cdot g^{-1}$. *J. Mater. Chem.* **2011**, *21*, 10179–10188.

[54] Lee, H. J.; Park, Y. J. Synthesis of $Li[Ni_{0.2}Li_{0.2}Mn_{0.6}]O_2$ nano-particles and their surface modification using a polydopamine layer. *J. Power Sources* **2013**, *244*, 222–233.

[55] Ye, D.; Ozawa, K.; Wang, B.; Hulicova-Jurcakova, D.; Zou, J.; Sun, C.; Wang, L. Capacity-controllable Li-rich cathode materials for lithium-ion batteries. *Nano Energy* **2014**, *6*, 92–102.

[56] Croy, J. R.; Kim, D.; Balasubramanian, M.; Gallagher, K.; Kang, S. H.; Thackeray, M. M. Countering the voltage decay in high capacity $x Li_2MnO_3 \cdot (1-x) LiMO_2$ electrodes (M = Mn, Ni, Co) for Li^+-ion batteries. *J. Electrochem. Soc.* **2012**, *159*, A781–A790.

[57] Martha, S. K.; Nanda, J.; Veith, G. M.; Dudney, N. J. Electrochemical and rate performance study of high-voltage lithium-rich composition: $Li_{1.2}Mn_{0.525}Ni_{0.175}Co_{0.1}O_2$. *J. Power Sources* **2012**, *199*, 220–226.

[58] Lee, E. S.; Manthiram, A. Smart design of lithium-rich layered oxide cathode compositions with suppressed voltage decay. *J. Mater. Chem. A* **2014**, *2*, 3932–3939.

[59] Croy, J. R.; Gallagher, K. G.; Balasubramanian, M.; Chen, Z.; Ren, Y.; Kim, D.; Kang, S. H.; Dees, D. W.; Thackeray, M. M. Examining hysteresis in composite $x Li_2MnO_3 \cdot (1-x) LiMO_2$ cathode structures. *J. Phys. Chem. C* **2013**, *117*, 6525–6536.

[60] Gu, M.; Belharouak, I.; Zheng, J.; Wu, H.; Xiao, J.; Genc, A.; Amine, K.; Thevuthasan, S.; Baer, D. R.; Zhang, J. G. Formation of the spinel phase in the layered composite cathode used in Li-ion batteries. *ACS Nano* **2012**, *7*, 760–767.

[61] Toprakci, O.; Toprakci, H. A.; Li, Y.; Ji, L.; Xue, L.; Lee, H.; Zhang, S.; Zhang, X. Synthesis and characterization of $x Li_2MnO_3 \cdot (1-x) LiMn_{1/3}Ni_{1/3}Co_{1/3}O_2$ composite cathode materials for rechargeable lithium-ion batteries. *J. Power Sources* **2013**, *241*, 522–528.

[62] Dong, X.; Xu, Y.; Xiong, L.; Sun, X.; Zhang, Z. Sodium substitution for partial lithium to significantly enhance the cycling stability of Li_2MnO_3 cathode material. *J. Power Sources* **2013**, *243*, 78–87.

[63] Rana, J.; Stan, M.; Kloepsch, R.; Li, J.; Schumacher, G.; Welter, E.; Zizak, I.; Banhart, J.; Winter, M. Structural changes in Li_2MnO_3 cathode material for Li-ion batteries. *Adv. Energy Mater.* **2014**, *4*, 1300998.

[64] Lee, K. T.; Jeong, S.; Cho, J. Roles of surface chemistry on safety and electrochemistry in lithium ion batteries. *Acc. Chem. Res.* **2012**, *46*, 1161–1170.

[65] Park, K. S.; Benayad, A.; Park, M. S.; Choi, W.; Im, D. Suppression of O_2 evolution from oxide cathode for lithium-ion batteries: VO_x-impregnated $0.5Li_2MnO_3$–$0.5LiNi_{0.4}Co_{0.2}Mn_{0.4}O_2$ cathode. *Chem. Commun.* **2010**, *46*, 4190–4192.